

Spartus: A 9.4 TOP/s FPGA-based LSTM Accelerator Exploiting Spatio-Temporal Sparsity

Chang Gao, *Student Member, IEEE*, Tobi Delbruck, *Fellow, IEEE* and Shih-Chii Liu, *Senior Member, IEEE*

Abstract—Long Short-Term Memory (LSTM) recurrent networks are frequently used for tasks involving time sequential data such as speech recognition. However, it is difficult to deploy these networks on hardware to achieve high throughput and low latency because the fully connected structure makes LSTM networks a memory-bounded algorithm. Previous LSTM accelerators either exploited weight spatial sparsity or temporal activation sparsity. This paper proposes a new accelerator called “Spartus” that exploits spatio-temporal sparsity to achieve ultra-low latency inference. The spatial sparsity is induced using our proposed pruning method called Column-Balanced Targeted Dropout (CBTD), which structures sparse weight matrices for balanced workload. It achieved up to 96% weight sparsity with negligible accuracy difference for an LSTM network trained on a TIMIT phone recognition task. To induce temporal sparsity in LSTM, we create the DeltaLSTM by extending the previous DeltaGRU method to the LSTM network. This combined sparsity simultaneously saves on the weight memory access and associated arithmetic operations. Spartus was implemented on a Xilinx Zynq-7100 FPGA. The Spartus per-sample latency for a single DeltaLSTM layer of 1024 neurons averages 1 μ s. Spartus achieved 9.4 TOP/s effective batch-1 throughput and 1.1 TOP/J energy efficiency, which, respectively, are 4X and 7X higher than the previous state-of-the-art.

Index Terms—FPGA, LSTM, weight sparsity, temporal sparsity, spatio-temporal sparsity

I. INTRODUCTION

RECURRENT Neural Networks (RNNs) are widely used in tasks involving temporal sequences. RNN variants used neuron models such as Long Short Term Memory (LSTM) [1] and Gated Recurrent Unit (GRU) [2] with additional gating units that help to mitigate the vanishing gradient problem. These models achieve state-of-the-art prediction accuracy in sequential tasks such as automatic speech recognition [3], [4], and natural language processing [5]. RNNs are also useful in latency-critical real-time control tasks, such as prosthesis [6], gaming AI [7] and autonomous driving [8], where ultra low batch-1 latency enables many inference cycles per data sample, thus enabling rapid gradient-descent optimization cycles for tasks such as model-predictive control.

Matrix-vector multiplication (MxV) is the dominant source of RNN computes. Its compute cost grows quadratically with a linear increase in RNN layers. The reasons why it is difficult to

achieve both low latency during RNN hardware inference are four-fold. First, the temporal dependency between the current RNN output and its previous output creates a critical path that limits parallelism between time steps. Second, large RNNs are essential for high accuracy, leading to a big weight memory footprint. Third, MxV is a memory-bounded operation. To compute MxV in each time step of an RNN, the underlying computing hardware must repeatedly execute sequential reads of large weight matrices from memory, and the weights are only used once per sample. Fourth, fetching data from memory consumes at least 10x more energy than the energy cost of the arithmetic units [9]. In short, the key to achieving low-latency RNN inference is to reduce the memory bottleneck, that is, to reduce the needed access of weights.

A popular method of reducing the memory access is to sparsify the weight matrices. Pruning methods [10]–[12] remove unimportant connections between neurons, resulting in sparse weight matrices with smaller memory footprint compared to the original dense matrices. Structured pruning was later introduced in RNN accelerators to address the problem of workload imbalance caused by irregular weight sparsity patterns after pruning [13]–[15]. Structured weight matrices [16]–[18], such as block-circulant matrices, reduce the effective number of weight parameters and enable the use of Fast Fourier Transform to reduce MxV cost from $\mathcal{O}(n^2)$ to $\mathcal{O}(n \log(n))$ [17].

Another way of reducing memory access requirements is to increase the temporal sparsity of the activations, as in spiking neural networks. The Delta Network (DN) algorithm was introduced as a method to induce temporal sparsity in deep networks by replacing state vectors with delta vectors that contain the temporal difference of states between two adjacent time steps [19]. By incorporating in addition, hardware that can skip zeros in the delta state vectors, we can remove the operations of entire columns of the weight matrix, which is intrinsically workload balanced [20], [21]. Temporal sparsity is similar to activation sparsity, which is popularly exploited in Convolutional Neural Networks (CNN) [22], [23] but rarely used in RNNs. Moreover, quantization of weights and states [24] can be combined with other methods to further reduce the model size.

As for the DN algorithm, columns of weights that are not skipped over are still dense. There is an opportunity to further reduce the memory footprint by inducing weight sparsity in a delta recurrent neural network. However, it is challenging to be implemented efficiently because the hardware has to deal with the irregular sparsity pattern in both delta state vectors and weight matrices. Moreover, since the sparsity pattern in

C. Gao, T. Delbruck and S-C. Liu are with the Institute of Neuroinformatics, University of Zurich and ETH Zurich, Zurich, Switzerland, 8057 Switzerland (email: chang@ini.uzh.ch; shih@ini.uzh.ch; tobi@ini.uzh.ch).

This work was supported by Samsung Advanced Institute of Technology (SAIT), University of Zurich and ETH Zurich. We thank Chen Xi for the discussion on the general concepts of the design. We also thank other Sensors Group members for their support on this work.

delta state vectors is dynamically updated online, the sparse matrix has to be properly structured and formatted to ensure good workload balance.

Previous RNN hardware accelerators only exploit either spatial sparsity [11], [14], [15], [17], [18] or temporal sparsity [20], [21]. It is challenging to exploit both sparsity types simultaneously because the hardware has to deal with the static sparsity pattern in weights and the dynamical sparsity pattern in states at the same time. Handling both sparsity types creates an extra level of complexity in achieving a good workload balance. In this paper, we describe an accelerator that achieves a further speedup of LSTM inference by exploiting spatio-temporal sparsity in both weights and states of the network. The main contributions of this work are:

- 1) We introduce a structured pruning method called Column-Balanced Targeted Dropout (**CBTD**) that produces a balanced workload among columns of a weight matrix; CBTD achieved up to 96% weight sparsity of an LSTM network without accuracy loss on a TIMIT phone recognition task.
- 2) We propose the DeltaLSTM by applying the delta network algorithm [19] to induce temporal sparsity in an LSTM network.
- 3) We present the first hardware LSTM-RNN accelerator, Spartus, that exploits both spatial and temporal sparsity in LSTM. The LSTM weight matrices are encoded in our customized sparse matrix format called Column-Balanced Compressed Sparse Column (**CBCSC**) that can be efficiently processed by the hardware. Spartus achieved 1 μ s inference latency of an LSTM layer with 4.7 million parameters. The accelerator achieved 9.4 Top/s effective batch-1 throughput and 1.1 Top/J energy efficiency, which are respectively 4X and 7X higher than the previous state-of-the-art.

II. LONG SHORT-TERM MEMORY (LSTM)

As shown in Fig. 1, an LSTM unit is composed of an input gate i , a forget gate f , a cell gate g , an output gate o , and a memory cell state c . Gates i , f , g control the update of the cell c state. Gate o determines the proportion of cell memory that is transferred to the hidden state output h . In a layer of multiple LSTM units, a gate in any unit receives two sequences of input vectors with sequence length T , including a sequence of external stimuli $X = \{\mathbf{x}_t | 1 \leq t \leq T, t \in \mathbb{N}\}$ and a sequence of previous hidden states $H_{in} = \{\mathbf{h}_t | 0 \leq t \leq T-1, t \in \mathbb{N}\}$ from the unit itself. At each time step, the LSTM layer generates a new hidden state vector giving a sequence $H_{out} = \{\mathbf{h}_t | 1 \leq t \leq T, t \in \mathbb{N}\}$.

The formulations of a vanilla LSTM layer are given as:

$$\begin{aligned}
 \mathbf{i}_t &= \sigma(\mathbf{W}_{ii}\mathbf{x}_t + \mathbf{b}_{ii} + \mathbf{W}_{hi}\mathbf{h}_{t-1} + \mathbf{b}_{hi}) \\
 \mathbf{f}_t &= \sigma(\mathbf{W}_{if}\mathbf{x}_t + \mathbf{b}_{if} + \mathbf{W}_{hf}\mathbf{h}_{t-1} + \mathbf{b}_{hf}) \\
 \mathbf{g}_t &= \tanh(\mathbf{W}_{ig}\mathbf{x}_t + \mathbf{b}_{ig} + \mathbf{W}_{hg}\mathbf{h}_{t-1} + \mathbf{b}_{hg}) \\
 \mathbf{o}_t &= \sigma(\mathbf{W}_{io}\mathbf{x}_t + \mathbf{b}_{io} + \mathbf{W}_{ho}\mathbf{h}_{t-1} + \mathbf{b}_{ho}) \\
 \mathbf{c}_t &= \mathbf{f}_t \odot \mathbf{c}_{t-1} + \mathbf{i}_t \odot \mathbf{g}_t \\
 \mathbf{h}_t &= \mathbf{o}_t \odot \tanh(\mathbf{c}_t)
 \end{aligned} \tag{1}$$

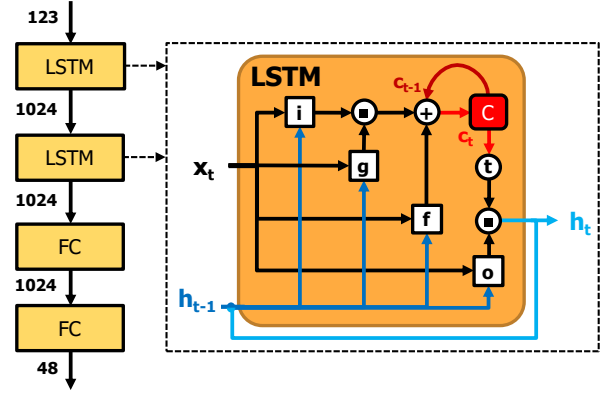


Fig. 1: Architecture of the LSTM network for an end-to-end automatic speech recognition task and internal structure of an LSTM unit

where W denote weight matrices, b denotes bias vectors. σ and \tanh are respectively the logistic sigmoid function and the hyperbolic trigonometric function. The symbol \odot signifies point-wise multiplication.

III. DELTALSTM

The delta network algorithm [19] was inspired by the neuromorphic principle that neurons have sparse activity transmission and it can be understood as follows. Given an input sequence, $X = \{\mathbf{x}_t | 1 \leq t \leq T, t \in \mathbb{N}\}$, the output is given by $Y = \{\mathbf{y}_t | 1 \leq t \leq T, t \in \mathbb{N}\}$:

$$\begin{aligned}
 \mathbf{y}_t &= \mathbf{W}\mathbf{x}_t \\
 \mathbf{y}_t &= \mathbf{W}\Delta\mathbf{x}_t + \mathbf{y}_{t-1}
 \end{aligned} \tag{2}$$

where $\Delta\mathbf{x}_t = \mathbf{x}_t - \mathbf{x}_{t-1}$ is the difference between input sequence elements from adjacent time steps and is called a delta vector. W is the matrix of weight connections from the input to the neurons. The delta vector can be sparse if all its elements below a delta threshold Θ are set to zero; thus, the term $\mathbf{W}\Delta\mathbf{x}$ in Eq. (2) becomes a dense matrix and sparse vector multiplication, in which Multiply-Accumulate (**MAC**) operations in matrix columns that correspond to zero delta vector elements can be skipped to reduce weight memory access.

Using Eq. 2, the LSTM equations, Eqs 1 are converted to their delta network version, called DeltaLSTM, following the formulations in Eq. 3:

$$\begin{aligned}
 \mathbf{D}_{i,t} &= \mathbf{W}_{ii}\Delta\mathbf{x}_t + \mathbf{W}_{hi}\Delta\mathbf{h}_{t-1} + \mathbf{D}_{i,t-1} \\
 \mathbf{D}_{f,t} &= \mathbf{W}_{if}\Delta\mathbf{x}_t + \mathbf{W}_{hf}\Delta\mathbf{h}_{t-1} + \mathbf{D}_{f,t-1} \\
 \mathbf{D}_{g,t} &= \mathbf{W}_{ig}\Delta\mathbf{x}_t + \mathbf{W}_{hg}\Delta\mathbf{h}_{t-1} + \mathbf{D}_{g,t-1} \\
 \mathbf{D}_{o,t} &= \mathbf{W}_{io}\Delta\mathbf{x}_t + \mathbf{W}_{ho}\Delta\mathbf{h}_{t-1} + \mathbf{D}_{o,t-1} \\
 \mathbf{i}_t &= \sigma(\mathbf{D}_{i,t}) \\
 \mathbf{f}_t &= \sigma(\mathbf{D}_{f,t}) \\
 \mathbf{g}_t &= \tanh(\mathbf{D}_{g,t}) \\
 \mathbf{o}_t &= \sigma(\mathbf{D}_{o,t}) \\
 \mathbf{c}_t &= \mathbf{f}_t \odot \mathbf{c}_{t-1} + \mathbf{i}_t \odot \mathbf{g}_t \\
 \mathbf{h}_t &= \mathbf{o}_t \odot \tanh(\mathbf{c}_t)
 \end{aligned} \tag{3}$$

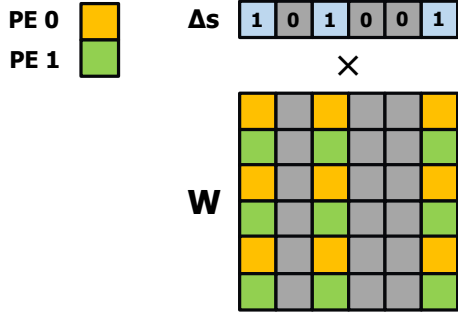


Fig. 2: Example of matrix-vector multiplication in Spartus between the weight matrix, W , and the delta state vector, Δs . The workload assignment of 2 PEs is shown here. Skipped columns due to zeros in Δs are highlighted in gray.

where the terms \mathbf{D} denote delta memory for each gate that are $M \times V$ results accumulated through time during LSTM inference. Delta memory terms in DeltaLSTM at $t = 1$ correspond to bias terms in LSTM and they are initialized to zeros. Because the delta threshold forces partial elements of delta vectors to be zeros, two vectors $\hat{\mathbf{x}}_{t-1}$ and $\hat{\mathbf{x}}_{t-1}$ are used to store the correct previous states to prevent accumulating errors in delta memories. Elements of $\hat{\mathbf{x}}_{t-1}$ and $\hat{\mathbf{x}}_{t-1}$ are updated only when their corresponding delta vector elements are above-threshold. The delta vector update process is defined by Eqs. 4~7.

$$\Delta \mathbf{x}_t = \begin{cases} \mathbf{x}_t - \hat{\mathbf{x}}_{t-1} & , |\mathbf{x}_t - \hat{\mathbf{x}}_{t-1}| > \Theta \\ 0 & , |\mathbf{x}_t - \hat{\mathbf{x}}_{t-1}| \leq \Theta \end{cases} \quad (4)$$

$$\hat{\mathbf{x}}_{t-1} = \begin{cases} \mathbf{x}_{t-1} & , |\mathbf{x}_t - \hat{\mathbf{x}}_{t-1}| > \Theta \\ \hat{\mathbf{x}}_{t-2} & , |\mathbf{x}_t - \hat{\mathbf{x}}_{t-1}| \leq \Theta \end{cases} \quad (5)$$

$$\Delta \mathbf{h}_{t-1} = \begin{cases} \mathbf{h}_{t-1} - \hat{\mathbf{h}}_{t-2} & , |\mathbf{h}_{t-1} - \hat{\mathbf{h}}_{t-2}| > \Theta \\ 0 & , |\mathbf{h}_{t-1} - \hat{\mathbf{h}}_{t-2}| \leq \Theta \end{cases} \quad (6)$$

$$\hat{\mathbf{h}}_{t-2} = \begin{cases} \mathbf{h}_{t-2} & , |\mathbf{h}_{t-1} - \hat{\mathbf{h}}_{t-2}| > \Theta \\ \hat{\mathbf{h}}_{t-3} & , |\mathbf{h}_{t-1} - \hat{\mathbf{h}}_{t-2}| \leq \Theta \end{cases} \quad (7)$$

The complete DeltaLSTM equation set is formed by Eq. 3 and Eqs. 4~7.

IV. STRUCTURED PRUNING OF DELTALSTM

The delta network algorithm converts dense-matrix-dense-vector multiplication in LSTM to dense-matrix-sparse-vector multiplication to save columns of $M \times V$ operations, but the remaining columns are still dense. These dense columns can be sparsified using pruning. However, random access of weight matrix columns is required to exploit temporal sparsity in delta state vectors and leads to difficulties in further exploiting sparsity in weight columns; that is, parallelizing MAC operations for hardware Processing Elements (PE) on remaining nonzero elements.

Fine-grain pruning methods [10] achieved high sparsity around 90% in RNN weights with negligible accuracy loss but introduce irregular nonzero element distribution that leads to imbalanced workload for PEs. Another pruning method called Bank-Balanced Sparsity (BBS) [14] first splits the rows of

a weight matrix into banks of equal lengths. Then, on each bank, a fine-grain pruning method applies the constraint that the number of nonzero elements in each bank must be the same. BBS can be used to obtain a sparse weight matrix that allows a balanced workload but cannot be efficiently applied to DeltaLSTM. In this case, we propose a hardware-oriented pruning method called Column-Balanced Targeted Dropout that makes workload balanced even with random weight column access in DeltaLSTM.

A. Column-Balanced Targeted Dropout (CBTD)

Algorithm 1: CBTD

Data: \mathbf{A} , matrix;

Q , the number of columns in \mathbf{A} ;

H , the height of columns in \mathbf{A} ;

γ , target sparsity;

α , dropout probability;

M , number of PEs allocated along a column.

Result: A sparse weight matrix \mathbf{B} of which columns having balanced workload for each PE;

Build set C containing all columns of \mathbf{A} , where

$$C = \{c_j | c_j \in \mathbb{R}^H, 1 \leq j \leq Q, j \in \mathbb{N}\};$$

Shuffle and split columns in set C into subcolumns

$$S\{s_{ij} | s_{ij} \in \mathbb{R}^{H/M}, 1 \leq i \leq M, 1 \leq j \leq Q, i, j \in \mathbb{N}\}$$

;

for $j = 1$ to Q **do**

for $i = 1$ to M **do**

 Sort elements of s_{ij} by their magnitudes;

 Set the smallest $H/M * \gamma$ elements in s_{ij} to zero with a probability of α ;

end

end

Reverse the shuffling and splitting to build a sparse matrix \mathbf{B} from subcolumns in set S ;

return \mathbf{B}

As shown in Fig. 2, interleaved rows of $M \times V$ workload are assigned to PEs that have MAC units for $M \times V$ computation in the Spartus accelerator. The procedure of applying CBTD on a weight matrix is shown in Algorithm 1. Given M , which is the number of PEs along the column direction in the Spartus accelerator, CBTD splits each column into the same number of groups called subcolumns as the number of PEs. Thus, M determines the size of each subcolumn for an LSTM layer of a certain size. Next, weight elements in each subcolumn are sorted by their magnitudes. Then, the smallest $H/M * \gamma$ portion of elements in each subcolumn is set to zero with a dropout probability α . γ is the target sparsity and the purpose of dropout probability α was used to introduce stochasticity into the targeted dropout process. The same γ and α are used for all subcolumns to make sure there is the same number of nonzero elements in each subcolumn. Therefore, M determines the granularity of CBTD. With a larger M , the locations of nonzero weights are tighter constrained due to the smaller subcolumn size and vice versa.

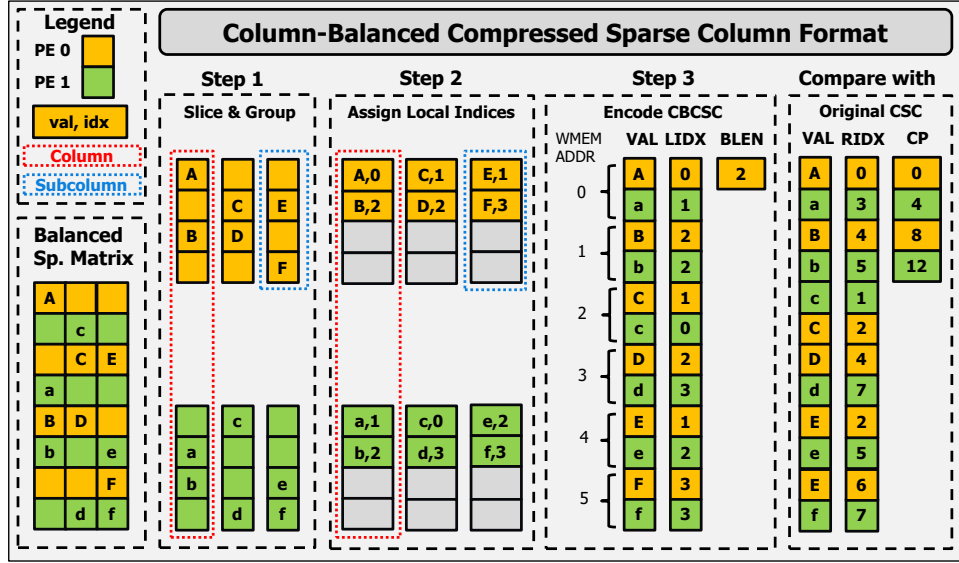


Fig. 3: Steps to encode a sparse matrix into the column-balanced compressed sparse column (CBCSC) format

Algorithm 2: LSTM Training with CBTD

Data: W , LSTM parameters;
 Q , the number of columns in W ;
 H , the height of columns in W ;
 γ , target sparsity;
 α , dropout probability;
 $\Delta\alpha$, step size of dropout probability;
 M , number of PE per column.

Result: Trained network with a sparse weight matrix of which columns having balanced workload for each PE;

```

while training do
   $\alpha = 0$ ;
  for epochs do
    Forward Propagation;
    Backward Propagation;
    Update Parameters  $W$ ;
    CBTD( $W$ ,  $Q$ ,  $H$ ,  $\gamma$ ,  $\alpha$ ,  $M$ );
    if  $\alpha < 1$  then
       $\alpha = \alpha + \Delta\alpha$ ;
    end
  end
end
end

```

B. LSTM Training with CBTD

CBTD should be applied to the training procedure of LSTM networks, which is described in Algorithm 2. The CBTD is used to set relatively unimportant weights to zeros in each epoch after the parameter update step. Weights that are set to zero in the previous epoch are allowed to recover during the parameter update step in the next epoch. The target sparsity γ is fixed throughout the training process. The dropout probability α is gradually incremented from 0 to 1 with a step size of $\Delta\alpha$, which determines after how many epochs the LSTM weight sparsity reaches the target value γ . This LSTM

Algorithm 3: CBCSC format Encoding

Data: A , a matrix;
 Q , the number of columns in A ;
 H , the height of columns in A ;
 M , the number of PEs in a MAC array;
 γ , target sparsity;

Result: Sparse matrix in CBCSC format stored in VAL , $LIDX$, $BLEN$;

Build set C containing all columns of A , where
 $C = \{c_j | c_j \in \mathbb{R}^H, 1 \leq j \leq Q, j \in \mathbb{N}\}$;
 Shuffle and split columns in set C into subcolumns
 $S\{s_{ij} | s_j \in \mathbb{R}^{H/M}, 1 \leq i \leq M, 1 \leq j \leq Q, i, j \in \mathbb{N}\}$;

```

for  $j = 1$  to  $Q$  do
  for  $i = 1$  to  $M$  do
    for  $k = 1$  to  $H/M$  do
      if  $s_{ij}[k] \neq 0$  then
         $VAL.append(s_{ij}[k])$ ;
         $LIDX.append(k)$ ;
      end
    end
  end
end
end
 $BLEN = \lceil H/M * (1 - \gamma) \rceil$ ;

```

training method guarantees that the network has the target sparsity and the same amount of nonzero elements between columns or between subcolumns at the end of the training.

C. Column-Balanced Compressed Sparse Column Format

V. ACCELERATOR DESIGN

To fully utilize the weight sparsity in an RNN pruned by CBTD, we propose a new sparse weight matrix format method called CBCSC based on the original CSC format [25]. A sparse matrix encoded in CBCSC has 3 vectors, *value* (VAL) for nonzero weight elements, *local index* (LIDX), and *column*

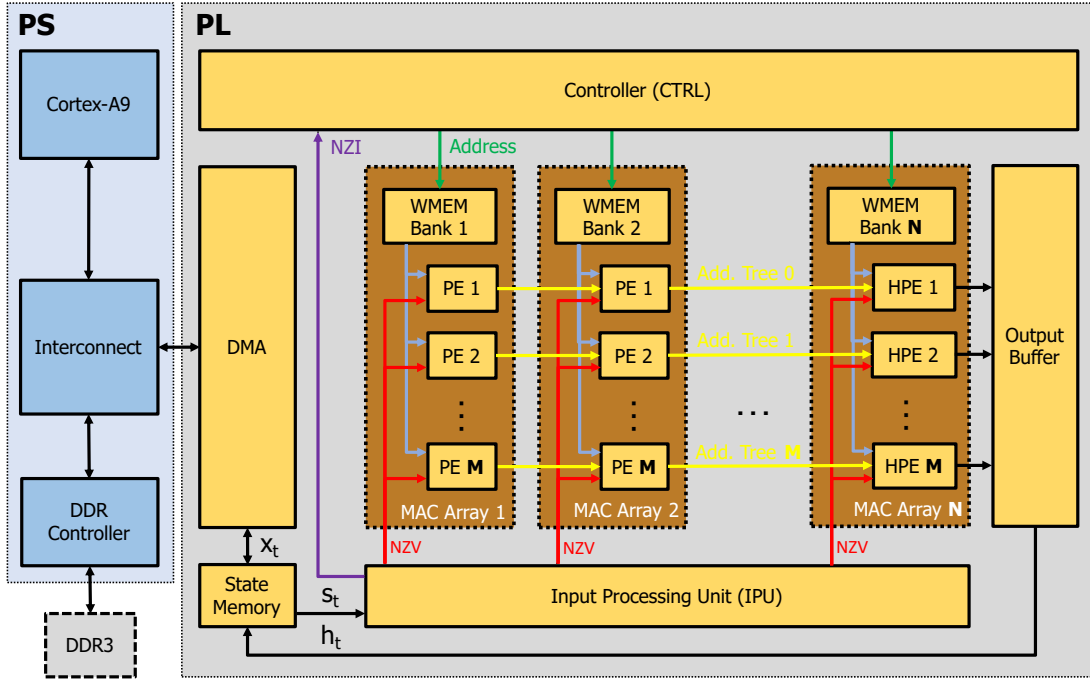


Fig. 4: Spartus accelerator system overview

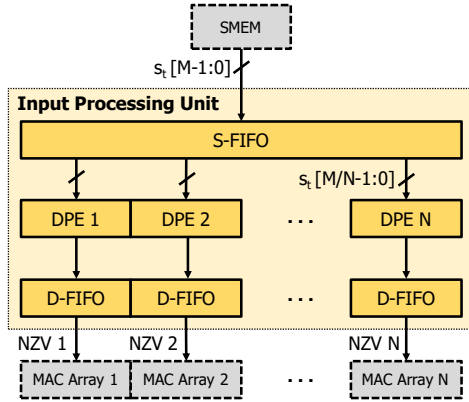


Fig. 5: Structure of the input processing unit

pointer (CP) that contains the indices of elements in VAL and RIDX that start new columns. The problem of CSC is that the nonzero elements are not arranged in a regular form that benefits PE access. During runtime, the number of weight elements for each PE at the memory interface, is different, making arbitration between PEs necessary to ensure correct dispatching of weights. The arbitration hurts the effective memory bandwidth for weight access. To overcome this problem, we proposed CBCSC to force the same number of weight elements for each PE at the memory interface. The procedure of CBCSC encoding is illustrated in Fig. 3 and steps are described below.

- 1) Assign interleaved rows to PEs. Columns of the weights matrix are sliced and interleaved elements in each column are grouped into subcolumns. Each subcolumn is assigned to a single PE.
- 2) Find the local index of each nonzero element within the

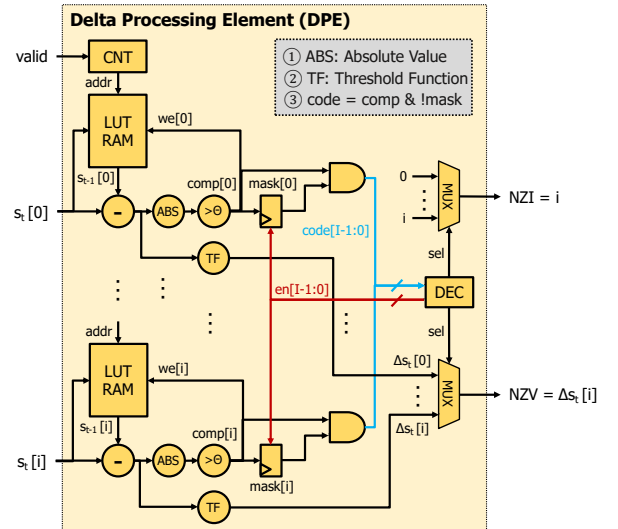


Fig. 6: Data flow of a delta processing element

subcolumn it resides in. Zero elements in each subcolumn are discarded and nonzero elements are aggregated into a dense vector.

- 3) Encode CBCSC by allocating nonzero values and corresponding indices into two vectors *value* (VAL), *local index* (LIDX). Another scalar value called burst length (BLEN) indicates the number of nonzero elements in each subcolumn. This process is described in Algorithm 3.

Compared with CSC, nonzero elements of the VAL vector in CBCSC are always aligned with the number of PEs, M , making it easy to dispatch weight data to corresponding PEs without arbitration and reduce logic area.

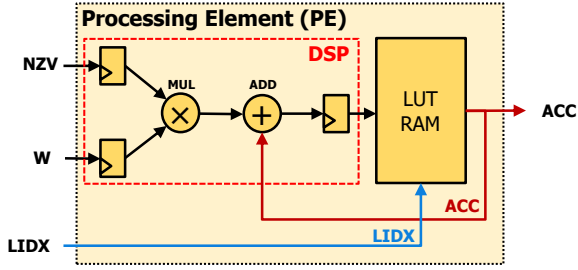


Fig. 7: Architecture of a processing element

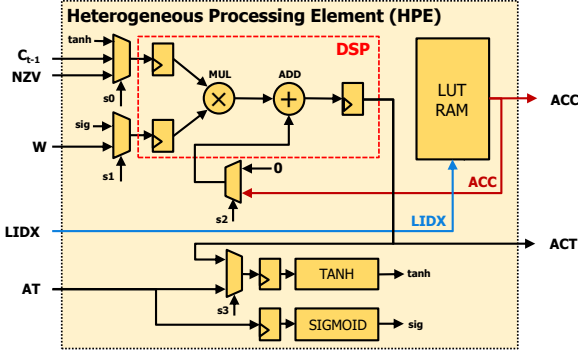


Fig. 8: Architecture of a heterogeneous processing element

A. Top-level Architecture

Fig. 4 shows the top-level architecture of the Spartus accelerator. The accelerator was implemented on the Programmable Logic (PL) of a Xilinx Zynq-7100 SoC, which also has an ARM Cortex-A9 CPU as the host on the Processing System (PS) side. Spartus is composed of a controller (CTRL), a State Memory (SMEM) block, an Input Processing Unit (IPU), MAC Arrays, Weight Memory (WMEM) Banks, Adder Trees (AT), and an Output Buffer. An Xilinx Direct Memory Access (DMA) IP block controlled by the host is used to manage I/O communications between the accelerator and the host. Input vectors, \mathbf{x}_t , are streamed from PS to PL through the DMA module and buffered in the SMEM block to hide the transfer latency. The SMEM block is also used to buffer LSTM activations \mathbf{h}_t . The IPU concatenates \mathbf{x}_t and \mathbf{h}_t to compute the delta state vectors Δs_t . The delta state vectors are encoded into Nonzero Values (NZVs) and Nonzero Indices (NZIs). NZIs are dispatched to CTRL to generate the physical memory addresses of weights in each WMEM bank, and NZVs are dispatched to MAC arrays to be multiplied to fetched weights. There are N MAC arrays. Each of the first $N - 1$ arrays contains M PEs that perform $M \times V$ between NZVs and corresponding weight columns. The last array has M heterogeneous processing elements (HPEs) that are also responsible for post- $M \times V$ activation generation. The output buffer (OB) helps to hide the latency of transferring the last layer's activations to the host.

B. Input Processing Unit (IPU)

The IPU computes delta state vectors Δs_t from both input vectors \mathbf{x}_t and hidden layer activations \mathbf{h}_t . It then generates

NZV and NZI that respectively contain the nonzero values of Δs_t and their corresponding indices. As shown in Fig 5, inputs of the IPU are streamed in from the SMEM block. In SMEM, the lengths of \mathbf{x}_t and \mathbf{h}_t vectors are zero-padded to the length that is a multiple of M and concatenated into a single state vector s_t . During the inference, the IPU receives M elements of s_t per clock cycle whenever the state FIFO (S-FIFO) is not full. The state vector $s_t[M - 1 : 0]$ is then partitioned into N equal segments $s_t[M/N - 1 : 0]$, each of which is fed into a Delta Processing Element (DPE) shown in Fig. 6. Details of the state vector partition will be discussed in Section V-E.

C. Delta Processing Unit (DPE)

Fig. 6 shows the architecture of the DPE. Following Eqs. 4~7, the DPE calculates a delta vector Δs_t with s_t and s_{t-1} . Each DPE receives a partitioned s_t segment of length $I = M/N$, given that M must be dividable by N . Input elements of a DPE are denoted as $S = \{s_t[i] | 0 \leq i \leq I-1, i \in \mathbb{N}\}$. s_t is buffered in the IPU input FIFO and s_{t-1} is stored in the look-up table based memory (LUTRAM) blocks in DPE. Each LUTRAM block is addressed by a counter (CNT), which is incremented by one when *valid* is asserted. Eq. 4 and Eq. 6 are implemented as the Threshold Function (TF) block while Eq. 5 and Eq. 7 are realized by controlling the write enable ($we[i]$) signal of the LUTRAM using the output of a comparator that produces a high logic state when $|\Delta s_t|$ is larger than the delta threshold Θ . Next, the first nonzero element in Δs_t with its index i are selected as NZV and NZI respectively by two multiplexers controlled by a decoder (DEC) according to signal $code[M/N-1:0]$. $code = comp \& mask$, where elements of $mask$ are initialized as ones. Controlled by the signal $en[i]$, when $mask[i] == 1$ and $comp[i] == 1$ in the current cycle, $mask[i]$ is overridden by zero in the next clock cycle. In this way, $mask$ is used to disable nonzero Δs_t once it is already selected and added into the NZV. The NZVs and NZIs generated from DPEs are buffered in their corresponding delta state FIFO (D-FIFO), which drives the input of PEs or HPEs in MAC arrays.

D. Multiply-Accumulate (MAC) Arrays

Sparse matrix and sparse vector multiplication (SpMxSpV) in Spartus are handled by the N MAC arrays. Each array receives NZVs from its corresponding DPE in the IPU. In Fig. 4, the left-most $N - 1$ MAC arrays have M PEs and the rightmost MAC array has M HPEs. As shown in Fig. 7, a PE has a MAC unit synthesized by a DSP block that performs up to 16-bit by 16-bit multiplication and 48-bit accumulations between NZVs and weights. Besides the DSP block, the HPE shown in Fig. 8 has multiplexers before each input operand of the DSP to reuse for point-wise multiplication and addition. Moreover, the HPE also has tanh and sigmoid blocks implemented in lookup tables.

Each PE or HPE has a dedicated LUTRAM block to buffer their corresponding partial sums. The LUTRAM is addressed by the IDX of weights encoded in the CBCSC format.

After SpMxSpV, delta memory terms DM defined in Eq. 3 are obtained by accumulating partial sums of all MAC arrays

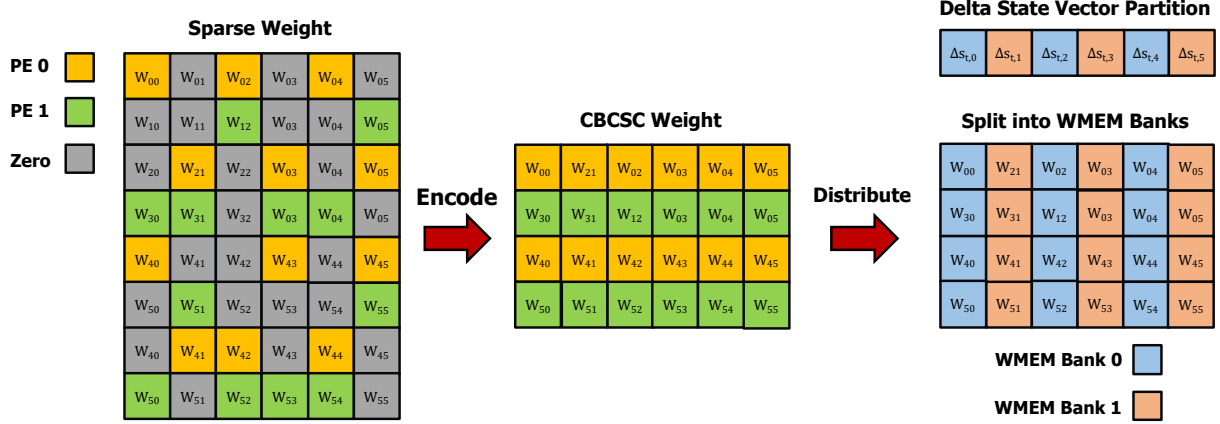


Fig. 9: Sparse DeltaLSTM weights are encoded into CBCSC format and then split into WMEM banks for each MAC array to access independently. This figure shows an example with $N = 2$ MAC arrays and $M = 2$ PEs/HPEs per array.

by M adder trees. Outputs of the adder trees are then fed to HPEs through the port AT for activation generation. Activation h_t are first stored in SMEM for delta state vector computation of the next time step and then streamed out to the host through DMA.

E. Network Adaptation

The Spartus accelerator supports fixed-point weights and activations. To run a DeltaLSTM network on Spartus, the network should be trained on GPU starting with floating-point parameters and quantized to fixed-point numbers before inference. To run an LSTM network with Spartus, weight matrices W_{ii} , W_{hi} , W_{if} , W_{hf} , W_{ig} , W_{hg} , W_{io} , W_{ho} are stacked in to a single matrix W_s given by Eq. 8.

$$W_s = \begin{pmatrix} W_{ii} & W_{hi} \\ W_{ig} & W_{hg} \\ W_{if} & W_{hf} \\ W_{io} & W_{ho} \end{pmatrix} \quad (8)$$

During matrix-vector multiplication, the stacked weight matrix is multiplied by the delta state vector Δs_t , which follows the same partition pattern as the state vector s_t . Accordingly, W_s is partitioned into N submatrices. Each submatrix only contains columns that will be multiplied by NZVs from its corresponding DPE and are encoded into the CBCSC format. As shown in Fig. 9, the sparse weights have to be encoded in CBCSC format as discussed in Section IV-C. Then, interleaved columns of the CBCSC weight are split into N submatrices. Each submatrix is stored in a WMEM bank dedicated to its corresponding MAC array to avoid bank conflict. The delta vector partition pattern follows how the stack weight matrix is split. The network weights are quantized to 8 bits. 8 bits are also used for their local indices (IDX) in the CBCSC format. In WMEM banks, weights and indices are concatenated into 16-bit words.

VI. EXPERIMENTAL SETUP

A. Hardware Implementation

The Spartus accelerator is synthesized and implemented in Vivado 2018.2 on the AVNET Zynq Mini-Module-Plus

System-on-Module that has a Xilinx Zynq XC7Z100 SoC. The SoC has a Dual ARM Cortex-A9 CPU in the PS as the host. The accelerator resides in the PL and is controlled by a bare-metal C program compiled in the Xilinx SDK. The program initializes LSTM weights in the DDR3 memory and then streams weights to the on-chip WMEM banks synthesized with Block RAMs (**BRAM**).

B. Feature Extraction & Network Setup

To evaluate the impact on the accuracy of the CBTD method and the DeltaLSTM algorithm on a speech recognition task, we trained a 2 layer LSTM network with 1024 neurons per layer as shown in Fig. 1. The LSTM layers are followed by a Fully Connected Layer (**FCL**) with 1024 neurons and a final logit layer. The Connectionist Temporal Classification (CTC) loss function [26] is used to train the network on a continuous end-to-end speech recognition task using the TIMIT corpus [27]. The dataset has the standard 462 speaker training set with all SA utterances removed, typically executed as in previous work [4]. The validation and test sets have utterances of 50 and 24 speakers respectively. 123-dimensional features extracted from the input consist of the 40 coefficients of FFT-based filter banks distributed on a mel-scale plus the energy term; and their first and second temporal derivatives. The networks to be implemented on Spartus hardware accelerator are quantized during training to 8-bit weights and 16-bit activation using the dual-copy rounding method [28].

C. Pretrain & Retrain

We adopted a pretrain-retrain process to train a network with spatio-temporal sparsity for this task. During the pretrain phase, vanilla LSTM layers were initialized and trained with the CBTD applied for 150 epochs. We set the growth rate of dropout probability $\Delta\alpha$ to 1/30 so that the target sparsity γ was achieved within the first 30 epochs and maintained during the remaining epochs. The CBTD was also applied to the FC layer with the same $\Delta\alpha$ and γ . The pretrain process was early stopped at the epoch that achieved the highest PER on the validation set.

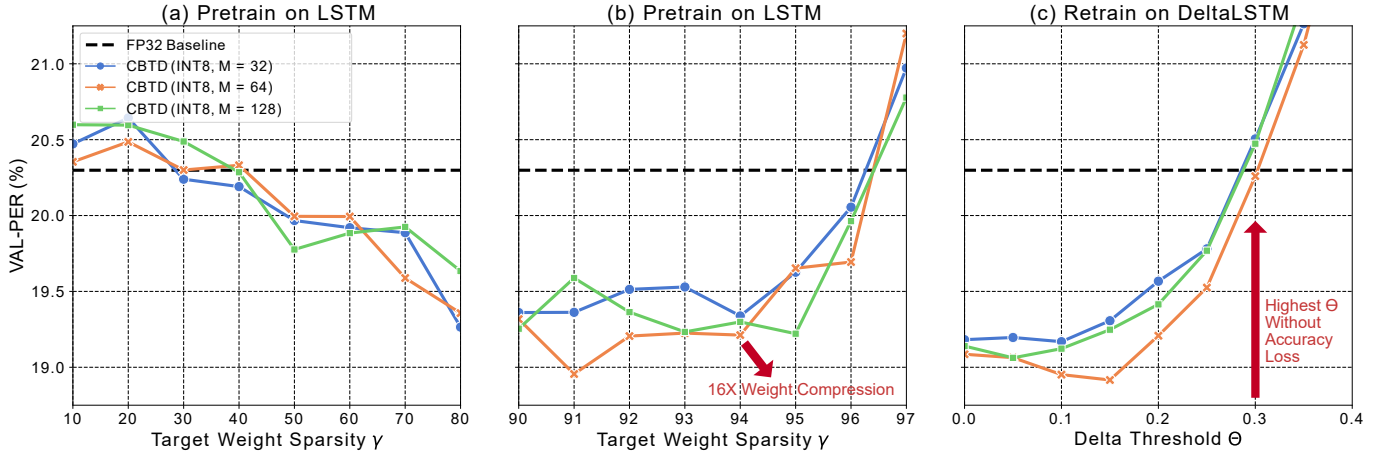


Fig. 10: Phoneme Error Rate (**PER**) evaluated on the TIMIT validation set (VAL-PER). (a) and (b) show change in PER with different target weight sparsity values after the 150-epoch pretrain phase on LSTM. (a) PER from $\gamma = 10\%$ to $\gamma = 80\%$ (step size = 10%). (b) PER from $\gamma = 90\%$ to $\gamma = 97\%$ (step size = 1%). (c) shows the change in PER after the 50-epoch retrain phase on DeltaLSTM for different delta thresholds. The pretrained models with 94% weight sparsity in (b) were used in the retrain phase. Results were averaged from 5 runs.

During the retrain phase, weights of the pretrained LSTM layers are copied into DeltaLSTM layers of the same size to be retrained for another 50 epochs with $\alpha = 1$. The retrain phase was also early stopped at the best validation PER. The final accuracy results are reported on the core test set which has 192 samples.

VII. RESULTS & DISCUSSION

A. Design Space Exploration

1) *Pretrain: Phone Error Rate vs. Weight Sparsity:* In this section, the impact of CBTD on weight sparsity and accuracy is studied. Fig. 10(a) & Fig. 10(b) show the evolution of PER on the validation set (VAL-PER) over the target sparsity. Each data dot in Fig. 10 is the average value out of 5 runs. We explored using different numbers of PEs per MAC array M with values of 32/64/128 for the CBTD method. The horizontal dashed line shows the VAL-PER of the network with 32-bit floating-point (FP32) parameters trained without using CBTD and quantization, which achieved 20.30% VAL-PER.

Results show that the accuracy with different numbers of PEs is similar. Most of the VAL-PER values of LSTM networks trained with CBTD were worse than the FP32 baseline when the target sparsity is below 40%. Similar to the Dropout [29] and Targeted Dropout [12] regularization methods, CBTD helped regularize the LSTM network. Target sparsity γ between 50% and 90% resulted in better VAL-PER than FP32 due to the regularization effect of CBTD. A similar regularization effect on the TIMIT dataset due to weight pruning on LSTM was also observed in [14]. The best PER results were achieved when γ was between 90% and 94%. The pretrained networks with CBTD achieved up to 96% weight sparsity without loss of accuracy when compared to the FP32 baseline results. To achieve the best PER while having speedup as high as possible, the network having 94% weights sparsity was used in the retrain phase, which achieved a VAL-

PER value of around 19.30% among the best PER values of all sparsity levels.

2) *Retrain: Phone Error Rate vs. Delta Threshold:* The purpose of the retrain phase is to induce temporal sparsity using the DeltaLSTM model. Temporal sparsity introduces zero elements that can be skipped to save the computations and the memory access but can lead to accuracy degradation once the sparsity is higher than a certain value. In this section, we report the results of the retrain phase and explore the optimal condition to achieve a balance between speedup and accuracy.

Fig. 10(c) shows the VAL-PER of the network retrained with DeltaLSTM layers. During the retrain phase, various delta thresholds Θ were used and the same thresholds are applied to all LSTM layers. The CBTD was still used during the whole training phase with a step size of dropout rate α fixed to 1. Results show that VAL-PER increases with increased delta thresholds Θ and the network trained with $M = 64$ achieved the best VAL-PER better than the FP32 baseline until $\Theta > 0.3$. Thus, we set $\Theta = 0.3$ to evaluate the performance of the accelerator.

3) *Workload Balance between MAC Arrays:* The theoretical peak throughput ν_{Peak} of the accelerator on the PL is given as:

$$\nu_{Peak} = 2 \cdot f_{pl} \cdot K \quad (9)$$

where f_{pl} is the operation clock frequency of the PL and K is the total number of MAC units. In Spartus, $K = M \times N$, where N is the number of MAC arrays. Thus, the theoretical peak throughput is proportional to the number of MAC arrays; however, the actual hardware throughput is affected by the workload imbalance between MAC arrays.

Unlike the structured sparse weight matrix induced by the CBTD method, the sparsity pattern of the delta state vector s_t is dynamically updated during LSTM inference in each time step. Therefore, partitioned Δs_t vector segments, which are encoded as NZVs by DPes, are likely to have different

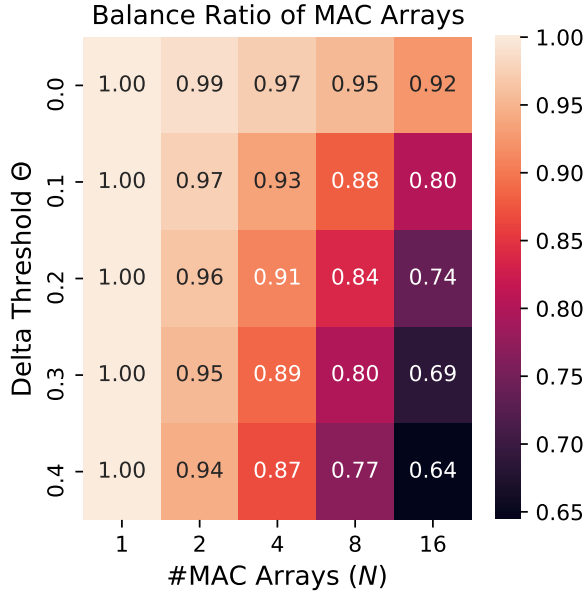


Fig. 11: Balance ratio of MAC arrays with respect to delta thresholds and different numbers of MAC arrays in the Spartus accelerator. The values were obtained by running the hardware over all TIMIT core test set samples.

numbers of nonzero values in each time step of the LSTM computation. Provided that there are N MAC arrays in the accelerator, the workload (WL), which is the number of nonzero elements of Δs_t allocated to the n -th MAC array at time step t , is WL_t^n . Then, the Balance Ratio (BR) of MAC arrays is given as:

$$BR = \frac{\sum_{t=1}^T WL_{t,mean}}{\sum_{t=1}^T WL_{t,max}} \quad (10)$$

$$WL_{t,mean} = \frac{\sum_{n=1}^N WL_t^n}{N}$$

$$WL_{t,max} = \max(WL_t^1, WL_t^2, \dots, WL_t^N)$$

where $WL_{t,mean}$ and $WL_{t,max}$ are respectively the mean and max workload of all MAC arrays at time step t . The BR is obtained by running the hardware on a temporal sequence with a length of T and getting the sum of $WL_{t,mean}$ and $WL_{t,max}$ over T time steps. The performance of hardware is bottlenecked by the max workload $WL_{t,max}$ at each time t . The optimal workload balance can be achieved once the workload of each MAC array equals to $WL_{t,mean}$. Therefore, the closer BR is to 1, the more balanced is the workload between MAC arrays.

Fig. 11 show the BR values of MAC arrays evaluated on all samples in the core test set of TIMIT running the best DeltaLSTM network selected after the retrain phase. When delta sparsity increased, the sparsity of the delta state vector was higher and resulted in the more imbalanced allocation of nonzero elements between MAC arrays. The workload is naturally more imbalanced when there are more MAC arrays in the hardware. To maximize the hardware performance at $\Theta = 0.3$, we considered setting the numbers of MAC array between

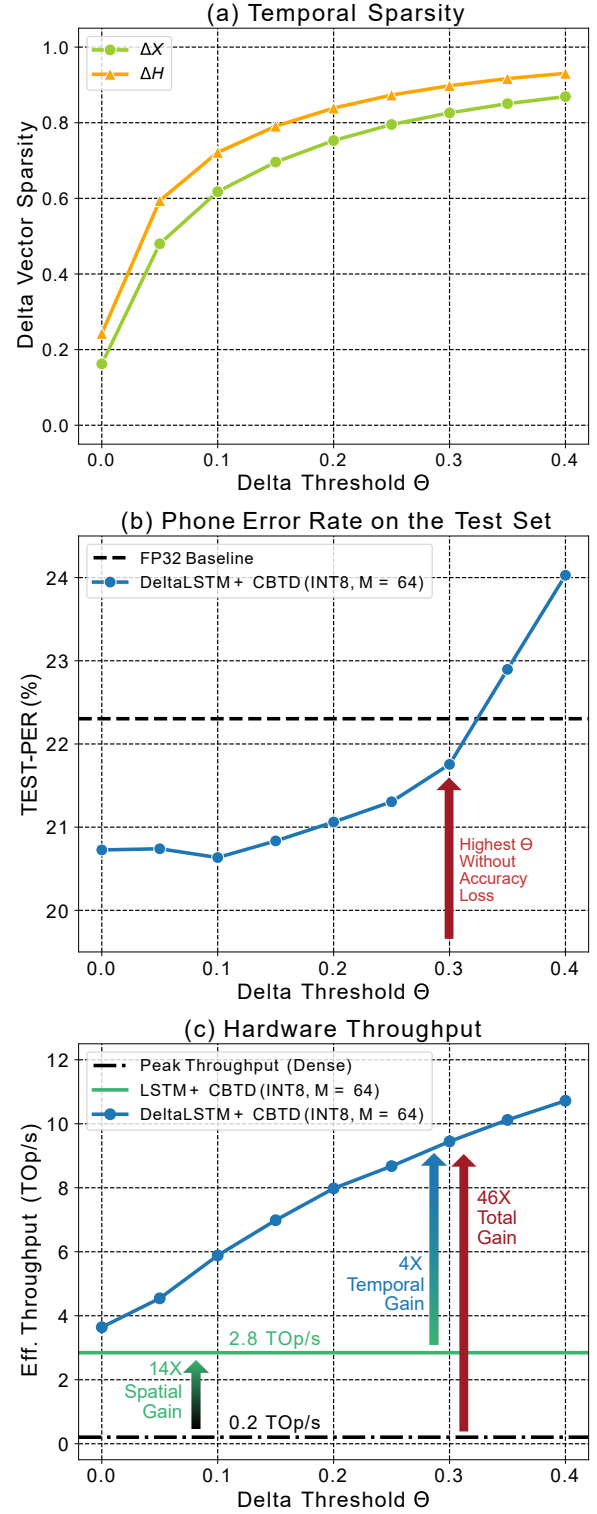


Fig. 12: (a) shows the PER of the DeltaLSTM network evaluated on the core test set of TIMIT; (b) shows the temporal sparsity of the DeltaLSTM network. Δx and Δh are respectively the delta input and delta hidden vectors; (c) shows the batch-1 throughput of the Spartus accelerator versus delta thresholds. The theoretical peak throughput is computed using Eq. 9.

TABLE I: XC7Z100 FPGA Resource utilization of Spartus

	LUT	FF	DSP	LUTRAM	BRAM
Available	277,400	554,800	2,020	108,200	755
Used	136,333	108,412	520	28,739	249
Percentage	49.15%	19.54%	25.74%	26.56%	32.98%

TABLE II: Summary of Spartus performance with progressive levels of optimization.

Optimizations	Settings	TEST-PER (%)	Batch-1 Eff. Throughput (GOp/s)	Latency (μ s)
FP32 Baseline	-	22.30 \pm 0.29	-	-
+Quantization	INT8	22.00 \pm 0.29	<204.80	>45.96
+CBTD	$\gamma = 94\%$ $M = 64$ $N = 8$	20.58 \pm 0.27	2845.44	3.32
+DeltaLSTM	$\Theta = 0.1$	20.63 \pm 0.30	5884.97	1.60
	$\Theta = 0.3$	21.75 \pm 0.30	9447.78	1.00

$N = 8$ and $N = 16$, where the BR value is between 0.8 and 0.69. Thus, the loss of hardware performance due to workload imbalance is between 20% to 31%, which is small compared to the 8X to 16X peak throughput gain by increasing N from 1 to 8 and 16. During our experiments, $N > 8$ resulted in congestion, making routing more difficult. Maximizing FPGA clock frequency was sacrificed for successful implementation on the target FPGA without timing violation. Therefore, we set $M = 64$ and $N = 8$ for our final Spartus implementation. The resource utilization of the XC7Z100 FPGA is summarized in Table I.

B. Model Evaluation on the Test Set

We evaluated the DeltaLSTM network trained with $M = 64$ in CBTD on the TIMIT core test set with different delta thresholds. Fig. 12(a) shows the temporal sparsity of delta input vector Δx and delta hidden vector Δh over the core test set and the values are the average temporal sparsity over the 2 DeltaLSTM layers. Overall, the sparsity of delta input state vector Δx is lower than delta hidden state vector Δh . This is due to the small temporal sparsity in the input layer of the whole network to allow enough input stimuli to be fed into the network. The delta hidden states can be up to 90% sparse when the threshold is larger than 0.3. Fig. 12(b) shows the PER on the core test set (TEST-PER) versus the delta threshold. The FP32 baseline on the test set was 22.30%. Similar to VAL-PER results, the DeltaLSTM network achieved better TEST-PER when the delta threshold Θ is smaller than 0.3. With small delta thresholds, the DeltaLSTM shows a slight regularization effect that helped to achieve the best TEST-PER at 20.63%. With $\Theta = 0.3$, the TEST-PER is 21.75% which corresponds to -0.55% accuracy degradation¹.

C. Hardware Performance: Throughput & Latency

Since we focus on achieving ultra-low latency LSTM inference, in this work, we evaluate the hardware throughput with a batch size of 1. Fig. 12(c) shows the effective batch-1 throughput of Spartus with respect to delta thresholds. Results

¹Negative accuracy degradation means the achieved PER is better than the baseline.

were obtained by running Spartus on all test samples in the core test set of TIMIT.

With $M \times N = 512$ MAC units, the baseline is the 0.2 TOP/s theoretical peak throughput obtained by Eq. 9. By applying only CBTD to the LSTM network to achieve 94% of weight sparsity (16X compression), the Spartus achieved 2.8 TOP/s batch-1 throughput, which is 14X speedup versus the baseline. After retraining the sparse LSTM layers as DeltaLSTM, further speedup was achieved. With a zero delta threshold, the accelerator was able to achieve 3.6 TOP/s batch-1 throughput. By increasing the delta threshold to 0.3, which is the highest value with better TEST-PER over FP32 baseline on TIMIT, the Spartus accelerator achieved 9.4 TOP/s batch-1 throughput, which is another 4X speedup compared to the throughput achieved with only using CBTD. Overall, by combining CBTD and DeltaLSTM, Spartus achieved 46X speedup over the baseline without losing accuracy.

Table II summarized the performance of Spartus with different levels of optimization and their corresponding accuracy on the TIMIT dataset. With the highest level of optimization, Spartus is able to finish the inference of the big DeltaLSTM layer within 1 μ s.

D. Comparison with previous work

We compare the performance of Spartus with previous state-of-the-art RNN accelerators on FPGA in Table III, including ESE [11], DeltaRNN [20], C-LSTM [17], E-RNN [18], BBS [14] and E-LSTM [15]. Except for DeltaRNN, all accelerators were tested by running a single-layer LSTM network with 1024 neurons. As for Spartus, we used the first LSTM layer, which has 4.7 million parameters, in the network shown in Fig. 1. ESE was the first RNN accelerator that adopted weight pruning to speedup LSTM inference. However, ESE was designed for throughput-oriented inference using large batch sizes. Performance of ESE was tested with a batch size of 32. DeltaRNN exploited temporal sparsity to accelerate GRU RNNs but the test network was small compared to other work. C-LSTM and E-RNN used a structured weight matrix with an FFT-based computing mechanism to reduce operations during inference. In Table III, we put performance numbers of C-LSTM and E-RNN with 16X compression ratio reported in the original papers. E-LSTM and BBS adopted structured pruning methods to achieve finer-grained workload balance compared to ESE and their performance was evaluated with batch sizes of 8 and 1 respectively. BBS achieved the best batch-1 throughput and latency among all the previous RNN accelerators. Since we focus on achieving low-latency LSTM inference, for a fair comparison, we computed the performance numbers of ESE and E-LSTM with a batch size of 1 in Table III. Power numbers of Spartus and other accelerators are measured wall-plug power of the FPGA board.

Except for DeltaRNN, all accelerators were tested on a single-layer LSTM with 1024 neurons. In Table III, we included 'Latency', 'Frame per Second (FPS)' to represent the performance of each accelerator on their own test networks. Spartus achieved the highest FPS and lowest inference latency among all platforms. However, the test network sizes are

TABLE III: Comparison with prior state-of-the-art RNN accelerators on FPGA (Batch Size = 1)

	ESE [11]	DeltaRNN [20]	C-LSTM [17]	E-RNN [18]	BBS [14]	E-LSTM [15]	Ours
Year	2017	2018	2018	2019	2019	2019	2021
FPGA	XCKU060	XC7Z100	7V3	7V3	GX1150	SX660	XC7Z100
Technology (nm)	20	28	28	28	20	20	28
#Parameters (M)	3.25	0.20	3.25	3.25	3.25	4.82	4.70
#Compressed Parameters (M)	0.36	N/A	0.20	0.20	0.41	0.60	0.29
Compression Ratio	9X	N/A	16X	16X	8X	8X	16X
PER Degradation (%)	0.30	N/A	0.32	0.31	0.25	-0.02	-0.55
Frequency (MHz)	200	125	200	200	200	200	200
Latency (us)	82.7	N/A	9.1	8.3	2.4	23.9	1.0
Frame per Second (KFPS)	12	N/A	110	120	417	42	1,001
Effective Throughput (GOp/s)	78.6	1198.0	714.3	783.1	2432.8	403.3	9447.8
Power (W)	41.0	7.3	23.0	25.0	19.1	15.9	8.4
Energy Efficiency (GOp/J)	1.9	164.1	31.1	31.3	127.4	25.4	1124.7

different across platforms. Spartus and E-LSTM used test networks with normal LSTM units, while ESE, C-LSTM, E-RNN, and BBS used a Google LSTM network with the same number of neurons but because their neuron model has peephole connections [30], this led to an overall decrease in the number of network parameters. Thus, we include 'Effective Throughput' and 'Energy Efficiency' metrics which take into the number of total operations for computing these networks in the comparison across these accelerators.

Compared to DeltaRNN which also exploited temporal sparsity, Spartus achieved 8X higher effective throughput and 7X higher energy efficiency. Compared to C-LSTM and E-RNN which achieved the same 16X weight compression ratio, Spartus achieved around 10X higher FPS and 8X lower latency. By exploiting spatio-temporal sparsity, Spartus achieved 4X higher batch-1 effective throughput than BBS which was the state-of-the-art accelerator with the highest batch-1 effective throughput.

VIII. CONCLUSION

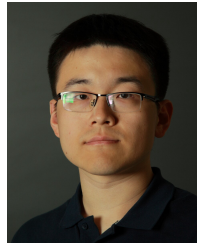
We proposed Spartus, the first LSTM accelerator that exploits spatio-temporal sparsity to enable the lowest latency and the highest energy efficiency in RNN inference compared to previous work. The spatial weight sparsity was implemented using our newly proposed structured CBTD pruning method. CBTD achieves a comparable compression rate as previous weight compression methods with negligible accuracy loss. The benefit of CBTD over previous methods is the compatibility with the DN algorithm. Temporal sparsity was achieved through the DeltaLSTM model by applying the delta network algorithm to the LSTM model. The Spartus accelerator was implemented on a Xilinx Zynq 7100 FPGA running at 200 MHz and achieved 9.4 TOP/s effective batch-1 throughput and 1.1 TOP/J energy efficiency, which is respectively 4X and 7X higher than the previous state-of-the-art. Compared to the theoretical peak hardware performance, which runs a dense LSTM layer with 1024 neurons in 46 μ s, Spartus runs the same network in 1 μ s by exploiting spatio-temporal sparsity, corresponding to 46X speedup. Exploiting spatio-temporal sparsity for other network types could also lead to increased energy efficiency and throughput during inference, which would be advantageous for resource-constrained edge devices.

REFERENCES

- [1] S. Hochreiter and J. Schmidhuber, "Long short-term memory," *Neural Comput.*, vol. 9, no. 8, pp. 1735–1780, Nov. 1997, ISSN: 0899-7667. DOI: 10.1162/neco.1997.9.8.1735.
- [2] K. Cho, B. van Merriënboer, Ç. Gülçehre, F. Bougares, H. Schwenk, and Y. Bengio, "Learning phrase representations using RNN encoder-decoder for statistical machine translation," *CoRR*, vol. abs/1406.1078, 2014. [Online]. Available: <http://arxiv.org/abs/1406.1078>.
- [3] D. Amodei, R. Anubhai, E. Battenberg, *et al.*, "Deep Speech 2: End-to-end speech recognition in english and mandarin," *CoRR*, vol. abs/1512.02595, 2015. [Online]. Available: <http://arxiv.org/abs/1512.02595>.
- [4] A. Graves, A.-r. Mohamed, and G. Hinton, "Speech recognition with deep recurrent neural networks," in *2013 IEEE international conference on acoustics, speech and signal processing*, Ieee, 2013, pp. 6645–6649.
- [5] T. Mikolov, M. Karafiát, L. Burget, J. Černocký, and S. Khudanpur, "Recurrent neural network based language model," in *Eleventh annual conference of the international speech communication association*, 2010.
- [6] C. Gao, R. Gehlhar, A. D. Ames, S.-C. Liu, and T. Delbruck, "Recurrent neural network control of a hybrid dynamical transfemoral prosthesis with EdgeDRNN accelerator," in *2020 IEEE International Conference on Robotics and Automation (ICRA)*, 2020, pp. 5460–5466. DOI: 10.1109/ICRA40945.2020.9196984.
- [7] O. Vinyals, I. Babuschkin, W. M. Czarnecki, *et al.*, "Grandmaster level in StarCraft II using multi-agent reinforcement learning," *Nature*, vol. 575, no. 7782, pp. 350–354, 2019, ISSN: 1476-4687. DOI: 10.1038/s41586-019-1724-z.
- [8] S. Mozaffari, O. Y. Al-Jarrah, M. Dianati, P. Jennings, and A. Mouzakitis, "Deep learning-based vehicle behavior prediction for autonomous driving applications: A review," *IEEE Transactions on Intelligent Transportation Systems*, pp. 1–15, 2020. DOI: 10.1109/TITS.2020.3012034.
- [9] M. Horowitz, "1.1 computing's energy problem (and what we can do about it)," in *2014 IEEE International Solid-State Circuits Conference Digest of Technical Papers (ISSCC)*, Feb. 2014, pp. 10–14. DOI: 10.1109/ISSCC.2014.6757323.
- [10] S. Han, H. Mao, and W. J. Dally, "Deep compression: Compressing deep neural network with pruning, trained quantization and Huffman coding," *CoRR*, vol. abs/1510.00149, 2015. arXiv: 1510.00149. [Online]. Available: <http://arxiv.org/abs/1510.00149>.
- [11] S. Han, J. Kang, H. Mao, *et al.*, "ESE: Efficient speech recognition engine with sparse LSTM on FPGA," in *Proceedings of the 2017 ACM/SIGDA International Symposium on Field-Programmable Gate Arrays*, ACM, 2017, pp. 75–84.
- [12] A. N. Gomez, I. Zhang, K. Swersky, Y. Gal, and G. E. Hinton, "Targeted dropout," in *2018 CDNNRIA Workshop at the 32nd Conference on Neural Information Processing Systems*, NeurIPS, 2018.
- [13] W. Wen, Y. He, S. Rajbhandari, *et al.*, "Learning intrinsic sparse structures within long short-term memory," in *International Conference on Learning Representations*, 2018. [Online]. Available: <https://openreview.net/forum?id=rk6cfpRjZ>.
- [14] S. Cao, C. Zhang, Z. Yao, *et al.*, "Efficient and effective sparse LSTM on FPGA with bank-balanced sparsity," in *Proceedings of the 2019 ACM/SIGDA International Symposium on Field-Programmable Gate*

Arrays, ser. FPGA '19, Seaside, CA, USA: ACM, 2019, pp. 63–72, ISBN: 978-1-4503-6137-8. DOI: 10.1145/3289602.3293898.

- [15] M. Wang, Z. Wang, J. Lu, J. Lin, and Z. Wang, “E-LSTM: An efficient hardware architecture for long short-term memory,” *IEEE Journal on Emerging and Selected Topics in Circuits and Systems*, vol. 9, no. 2, pp. 280–291, 2019. DOI: 10.1109/JETCAS.2019.2911739.
- [16] Z. Wang, J. Lin, and Z. Wang, “Accelerating recurrent neural networks: A memory-efficient approach,” *IEEE Transactions on Very Large Scale Integration (VLSI) Systems*, vol. 25, no. 10, pp. 2763–2775, Oct. 2017, ISSN: 1063-8210. DOI: 10.1109/TVLSI.2017.2717950.
- [17] S. Wang, Z. Li, C. Ding, *et al.*, “C-LSTM: Enabling efficient LSTM using structured compression techniques on FPGAs,” in *Proceedings of the 2018 ACM/SIGDA International Symposium on Field-Programmable Gate Arrays*, ser. FPGA '18, Monterey, CALIFORNIA, USA: ACM, 2018, pp. 11–20, ISBN: 978-1-4503-5614-5. DOI: 10.1145/3174243.3174253.
- [18] Z. Li, C. Ding, S. Wang, *et al.*, “E-RNN: Design optimization for efficient recurrent neural networks in FPGAs,” in *2019 IEEE International Symposium on High Performance Computer Architecture (HPCA)*, 2019, pp. 69–80. DOI: 10.1109/HPCA.2019.00028.
- [19] D. Neil, J. Lee, T. Delbrück, and S.-C. Liu, “Delta networks for optimized recurrent network computation,” in *Proceedings of the 34th International Conference on Machine Learning, ICML 2017, Sydney, NSW, Australia, 6-11 August 2017*, 2017, pp. 2584–2593. [Online]. Available: <http://proceedings.mlr.press/v70/neil17a.html>.
- [20] C. Gao, D. Neil, E. Ceolini, S.-C. Liu, and T. Delbrück, “DeltaRNN: A power-efficient recurrent neural network accelerator,” in *Proceedings of the 2018 ACM/SIGDA International Symposium on Field-Programmable Gate Arrays*, ser. FPGA '18, Monterey, CALIFORNIA, USA: ACM, 2018, pp. 21–30, ISBN: 978-1-4503-5614-5. DOI: 10.1145/3174243.3174261.
- [21] C. Gao, A. Rios-Navarro, X. Chen, S.-C. Liu, and T. Delbrück, “EdgeDRNN: Recurrent neural network accelerator for edge inference,” *IEEE Journal on Emerging and Selected Topics in Circuits and Systems*, vol. 10, no. 4, pp. 419–432, 2020. DOI: 10.1109/JETCAS.2020.3040300.
- [22] A. Aymar, H. Mostafa, E. Calabrese, *et al.*, “NullHop: A flexible convolutional neural network accelerator based on sparse representations of feature maps,” *IEEE Transactions on Neural Networks and Learning Systems*, vol. 30, no. 3, pp. 644–656, 2019. DOI: 10.1109/TNNLS.2018.2852335.
- [23] Q. Chen, Y. Huang, R. Sun, *et al.*, “An efficient accelerator for multiple convolutions from the sparsity perspective,” *IEEE Transactions on Very Large Scale Integration (VLSI) Systems*, vol. 28, no. 6, pp. 1540–1544, 2020. DOI: 10.1109/TVLSI.2020.2976454.
- [24] C. Xu, J. Yao, Z. Lin, *et al.*, “Alternating multi-bit quantization for recurrent neural networks,” in *International Conference on Learning Representations*, 2018. [Online]. Available: <https://openreview.net/forum?id=S19dR9x0b>.
- [25] I. S. Duff, R. G. Grimes, and J. G. Lewis, “Sparse matrix test problems,” *ACM Trans. Math. Softw.*, vol. 15, no. 1, pp. 1–14, Mar. 1989, ISSN: 0098-3500. DOI: 10.1145/62038.62043.
- [26] A. Graves, S. Fernández, F. Gomez, and J. Schmidhuber, “Connectionist temporal classification: Labelling unsegmented sequence data with recurrent neural networks,” in *Proceedings of the 23rd international conference on Machine learning*, ACM, 2006, pp. 369–376.
- [27] J. S. Garofolo, L. F. Lamel, W. M. Fisher, J. G. Fiscus, D. S. Pallett, and N. L. Dahlgren, *DARPA TIMIT acoustic phonetic continuous speech corpus cdrom*, 1993.
- [28] E. Stamatias, D. Neil, M. Pfeiffer, F. Galluppi, S. B. Furber, and S.-C. Liu, “Robustness of spiking deep belief networks to noise and reduced bit precision of neuro-inspired hardware platforms,” *Frontiers in Neuroscience*, vol. 9, p. 222, 2015, ISSN: 1662-453X. DOI: 10.3389/fnins.2015.00222.
- [29] N. Srivastava, G. Hinton, A. Krizhevsky, I. Sutskever, and R. Salakhutdinov, “Dropout: A simple way to prevent neural networks from overfitting,” *Journal of Machine Learning Research*, vol. 15, no. 56, pp. 1929–1958, 2014. [Online]. Available: <http://jmlr.org/papers/v15/srivastava14a.html>.
- [30] H. Sak, A. Senior, and F. Beaufays, “Long short-term memory recurrent neural network architectures for large scale acoustic modeling,” in *Fifteenth Annual Conference of the International Speech Communication Association*, 2014.



Chang Gao received the B.S. degree in Electronics from University of Liverpool, Liverpool, UK and Xi'an Jiaotong-Liverpool University, Suzhou, China, and the master's degree in analog and digital integrated circuit design from Imperial College London, London, UK. He is currently finishing his Doctoral degree at the Institute of Neuroinformatics, University of Zurich and ETH Zurich, Zurich, Switzerland. His current research interests include computer architectures for deep learning with emphasis on recurrent neural networks.



Tobi Delbruck (M'99–SM'06–F'13) received the B.Sc. degree in physics from the University of California at San Diego, San Diego, CA, USA, in 1986, and the Ph.D. degree from the California Institute of Technology, Pasadena, CA, USA, in 1993. Since 1998, he has been with the Institute of Neuroinformatics, University of Zurich and ETH Zurich, Zürich, Switzerland, where he is a Professor of physics and electrical engineering. His group along with S.-C. Liu focuses on neuromorphic sensory processing and efficient deep learning.



Shih-Chii Liu (M'02–SM'07) received the bachelor's degree in electrical engineering from the Massachusetts Institute of Technology, Cambridge, MA, USA, and the Ph.D. degree in the computation and neural systems program from the California Institute of Technology, Pasadena, CA, USA, in 1997. She was with various companies, including Gould American Microsystems, San Jose, CA, USA, LSI Logic, Sherman Oaks, CA, USA, and Rockwell International Research Labs, Thousand Oaks, CA, USA. She is Professor and Group Leader at the Institute of Neuroinformatics, University of Zurich and ETH Zurich, Zürich, Switzerland.